Characterization of rat vertebrae cortical bone microstructures using confocal Raman microscopy combined to tomography and electron microscopy

S.A. Shah, H. Salehi, Vincent Cavaillès, F. Fernandez, Frédéric Cuisinier, Pierre-Yves Collart Dutilleul, Alban Desoutter

Characterization of rat vertebrae cortical bone microstructures

using confocal Raman microscopy combined to tomography and electron microscopy

S.A. Shah[1], H. Salehi[1], V. Cavaillès[2], F. Fernandez[3], F. Cuisinier[1,4,5], P-Y. Collart-Dutilleul[1,4,5] and A. Desoutter[1]

1 LBN, Univ. Montpellier, Montpellier, France.

2 IRCM, INSERM U1194, Univ. Montpellier, Montpellier, France.

3 MEA, Univ. Montpellier, Montpellier, France.

3 UFR Odontologie, Univ. Montpellier, Montpellier, France.

4 Service Odontologie, CHU de Montpellier, Montpellier, France

Shahid Ali Shah, LBN, Univ. Montpellier, 545 avenue Professeur Jean-Louis Viala, 34193 Montpellier Cedex 5. Mail: dr_s.a.shah@live.com

Hamideh Salehi, LBN, Univ. Montpellier, 545 avenue Professeur Jean-Louis Viala, 34193 Montpellier Cedex 5. Mail: s_hamideh@yahoo.com

Vincent Cavaillès, Institut de Recherche en Cancérologie de Montpellier, 124 Av. des Apothicaires, 34090 Montpellier. Mail: vincent.cavailles@inserm.fr

Frederic Fernandez, MEA, Univ. Montpellier, Place Eugène bataillon, CC437 3409 Montpellier Cedex 5. Mail : frederic.feranandez@umontpellier.fr

Frédéric Cuisinier, LBN, Univ. Montpellier, 545 avenue Professeur Jean-Louis Viala, 34193 Montpellier Cedex 5. Mail: frederic.cuisinier@umontpellier.fr

Pierre Yves Collart-Dutilleul, Univ. Montpellier, 545 avenue Professeur Jean-Louis Viala, 34193 Montpellier Cedex 5. Mail: pierre-yves.collart-dutilleul@umontpellier.fr

Alban Desoutter, LBN, Univ. Montpellier, 545 avenue Professeur Jean-Louis Viala, 34193 Montpellier Cedex 5. Mail: alban.desoutter@umontpellier.fr

Abstract:

Background: The rat vertebrae is a good model to study bone regeneration after implantation of biomaterials used to treat bone loss, a major problem in oral and dental surgery. However, the precise characterization of bone microstructures in the rat vertebrae has not been reported. Therefore, the aim of this study was to achieve the complete analysis of such bone, at different scales**,** in order to have a clear model of healthy bone for comparison with regenerated bone.

Methods: In order to image the cortical bone of rat caudal vertebra, confocal Raman microscopy was combined to high resolution X-ray micro computed tomography (micro-CT), to scanning electron microscopy (SEM) using backscatter electron imaging and to more conventional histology coloration techniques. SEM and Raman microscopy were done in various regions of the cortical bone corresponding to external, middle and internal areas. The spongy bone was imaged in parallel. Micro-CT was performed on the whole vertebra to monitor the network of haversian canals in the cortical bone. Osteonic canals characteristics, and relative chemical composition were analysis in several region of interest, in cortical and spongy bone. 5 rats were included in this study.

Results: On micro-CT images, differences in intensity were observed in cortical bone, substantiated by SEM. Chemical analysis with Raman spectra confirmed the difference in composition between the different regions of the cortical and spongy bone. PCA and k-mean cluster analysis separated these groups, except for the external and middle cortical bone. Peak intensity ratio confirmed these results with a CO_3 to ν_2 PO_4 ratio significantly different for the internal cortical bone. Grayscale images stack extracted from micro-CT showed that global architecture of cortical bone was characterized by a dense and complex network of haversian osteonic canals, starting from the surface towards the vertebrae center. The mean diameter of the canals was 18.4 µm (SD 8.6 µm) and the mean length was 450 µm (SD 152 µm). Finally, Raman reconstructed images of the lamellar bone showed an enlargement of the lamellar layer width, both in circumferential lamellar bone and around haversian canals.

Conclusions: Micro-CT and confocal Raman microscopy are good tools to complete classical analysis using optical and electron microscopy. The results and measurements presented in a rat model known for its small inter-individual differences provide the main characteristics of a mature bone. This study will allow the community working on this rat

vertebrate model to have a set of characteristics, in particular on the structure of the haversian canals.

Keywords: Confocal Raman microscopy, high resolution micro tomography, rat vertebra, cortical bone structure, mineral density, Haversian canals, lamellar bone

1 Introduction

Bone is a complex structure, composed by anisotropic and viscoelastic microstructures owing to its hydroxyapatite and organic matrix phases, mainly formed of type-I collagen. Its principal function is to resist to mechanical forces and fractures (Viguet-Carrin et al., 2006). Bone is also a location of hemopoiesis. The composition of the mineral phase is close to that of tooth material, with hydroxyapatite poorly crystallized (unlike tooth enamel), collagen and protein content (Goldberg et al., 2011). The high mechanical strength of bone results from the intricate organization of cortical and spongy bone and from the reinforcement by the lamellar structure of mineralized collagen. At the mesoscopic scale, cortical bone is organized into osteons which consists of a central osteonic canal, previously named haversian canal surrounded by concentric lamellae. Lamellar bone is the most abundant bone in mammals and is composed of array of aligned mineralized fibrils of oriented collagen (Weiner et al., 1999). Lamellar bone could be found around osteonic canal but also in external part of cortical bone, also called circumferential lamellar bone (Liu et al., 2000). The osteonic canals are connected to each other by transverse canals (Volkmann canals), which are perpendicular to the former (Hall, 2005). This has been well described by classical histology using two dimension images of stained sections (Pritchard, 1972). Architecture and composition of each phase, together with the continuous dynamic remodeling along the life span, explain the very high resistance of bone to strain and fracture.

Bone structure and regeneration can be studied radiographically, with micro computerized tomography (µCT) (Gregor et al., 2012; Particelli et al., 2012; Kubíková et al., 2018) or by invasive techniques such as histology and scanning electron microscopy (SEM). Moreover, bone structure has been recently highlighted by confocal Raman microscopy (Moura et al., 2016). Several published works have presented new ways of data treatment, allowing results standardization and improving data analysis reproducibility (Unal et al., 2021). The combination of 3D imaging and Raman microscopy is considered as an efficient way to

assess bone quality and its regeneration during healing processes (Adachi et al., 2020), with potential *in vivo* applications (Gatin et al., 2022). Chemical mapping with Raman provides valuable information about mineral concentration, ratio between mineral and organic matrix phase, bone crystallinity or extended chemical composition (Shah, 2020). It also provides data concerning the orientation of mineral crystals, in relation to the axis of the collagen fibril (Khalid et al., 2018). Thus, Raman microscopy presents an interesting tool for studying biological systems (such as bone composition and regeneration), without chemical perturbation (Moura et al., 2016).

Indeed, Raman spectroscopy is based on the interaction between emitted light, by a laser source, and optical phonons representing the chemical bond of the studied material or biological structure. This coupling induces a particular light scattering, represented by particular wavelengths. For bone, peaks could be classified in two categories: ν_1 PO_4^{3-}, ν_2-PO_4^{3-}, ν_3 PO_4^{3-}, ν_4 PO_4^{3-}, and ν_1 CO_3^{2-} representing hydroxyapatite, and amide I, amide III, Proline, Hydroxyproline, Phenylalanine, $\delta(CH_3)$, $\delta(CH_2)$, and $\nu(CH)$ representing the organic elements. In addition, since Raman microscopy only gives relative values, the ratios between sample compositions are more accurate than the absolute values. This aspect is of particular importance because Raman peak intensities are very sensitive to the environment and difficult to precisely reproduce. Laser photobleaching effect has also an influence on peak intensities, but the ratios between the components remain robust and reproducible.

Three main other information about extracellular matrix composition could be obtained from these peak ratios. First, the mineral to matrix ratio, which is considered as the degree of mineralization (Morris & Mandair, 2011) can be evaluated by using the ν_4 PO_4/proline and $\nu4$ PO_4/amide III ratios (Nyman et al., 2011). The ν_1 CO_3 to PO_4 ratio measures B-type carbonate substitution, i.e. integration of CO_3 group instead of a PO_4^{3-} group. This ratio is correlated to carbonate percentage (Awonusi et al., 2007) or to bone age in the case of rat cortical model (Akkus et al., 2004; Raghavan et al., 2012). Finally, crystallinity is related to the width of PO_4^{3-} peak. The measure of invert of full width at half maximum of the peak gives information related to the degree of organization in a crystal-like structure, in opposition to amorphous material. In both mouse and human, subject's age is positively correlated to crystallinity (Freeman et al., 2001; Iwasaki et al., 2011; Nieuwoudt et al., 2020). In a study about lamellar bone orientation and composition by Raman microscopy, it has been shown that the ν_1 PO_4 to amide I ratio mainly quantifies lamellarity of bone orientation; ν_2 PO_4 to amide III and CO_3 to ν_2 PO_4 ratios display variation in bone composition (Kazanci et al., 2007).

Raman microscopy analysis combines chemical mapping with optical resolution but the refractive index of bone does not allow z stack, and scanned zones cannot exceed a square of 150 micrometers due to the limitation of piezo table. Therefore, the study of 3D organization of cortical bone microstructures like Haversian and Volkmann canals required additional tools, specifically investigating structure in the z-plane so that a 3D analysis could be made. Micro-CT with high resolution/small voxel size answered this need. Such analysis has already been done for cortical human bone with a 10 micrometers resolution micro-CT. Distribution of Havers canals diameter, connectivity and some parameters of bone like canal volume, number and density have been collected in human bone samples (Cooper et al., 2003). Rat vertebrae were also studied in micro-CT, to test stiffness of bone in particular, in an osteoporosis model (Frost & Jee, 1992), but without a 3D cortical canals microstructure analysis.

In the work presented here, we have combined several technics to study the cortical bone of the rat vertebrae, which is a good model to test bone regeneration materials (Renaud et al., 2016), in particular for the mandibular and maxillary bone. Several examples of rat vertebrae defect are found in literature (Renaud et al., 2016), used to evaluate mineralization, medical device as implant (Blazsek et al., 2009), stem cells (Sheyn et al., 2011) or biomaterial (Wang et al., 2008; Belaid et al., 2022).

We focused on rat tail vertebrae because of the similarities between the vertebral and mandibular bone, and because of the simplicity to access to the surgical site *in vivo*, with one animal allowing multiple assays on this model. Moreover, since the 90's, many studies have demonstrated the similarity in rat and human bone (Pearce et al., 2007; Weber et al., 2019), regarding their reaction to influences such as hormones, drugs . A good correlation in gain or losses of bone mass between rats and humans had also been highlighted (Frost & Jee, 1992).

To assess bone regeneration, the evaluation criteria are usually based on newly formed bone, in term of quality and quantity. Therefore, we aimed to bring insight about the qualitative evaluation of newly formed bone, by describing the 3D microstructure of the cortical bone of the rat vertebrae, focusing on bone composition and on the dynamic of the osteonic canals network. Our main objective was to provide a precise description of cortical and trabecular bone from the microanatomical and chemical point of view, to serve as reference for bone qualitative assessment. Therefore, we used chemical imaging by confocal Raman microscopy combined with high resolution µCT.

We hypothesized that it may be possible to distinguish cortical bone positioning according to its chemical signature and microanatomical structure. We specifically targeted (1) to characterize osteonic canals network, (2) to map the chemical composition of the different regions of cortical bone, and (3) to characterize lamellar bone ultrasructure. For that purpose, cortical bone was imaged in three different zones, by confocal Raman microscopy and SEM using backscatter electron imaging, to establish particulate hydroxyapatite and protein composition in the external, in the bulk/central, and in the internal part of bone. In parallel, the whole vertebra was scanned with high-resolution µCT following guidelines for bone microstructure assessment in rodents.

2 Material and method

2.1 Sample preparation

Five Wistar rats were included in the study: 3 males and 2 females, aged of 4 months and weighing between 196 and 135 g. After euthanasia, rat tails were collected and fixed in 4% formalin for 24 hours, washed 3 times in PBS, then cut to generate samples of approximately 1 cm long. These samples were first brought to analyze with µCT. After data acquisition, the samples were dehydrated through a 70%-100% alcohol series, then cleared through two changes of xylene. The specimens were progressively infiltrated with Technovit 9100 (T9100) and finally embedded in a polymerization solution of T9100 (Kulzer GmbH, Kulzer Technik, Wehrheim Germany) at -0.5°C in a freezer. Once the polymerization was complete, the blocks were brought to room temperature and removed from the molding containers. A precision saw (Isomet 2000, Buehler, USA) was used to cut 400 µm sections from the embedded samples. Each slice was polished with abrasive disk of 1200 then 2400 grit. Sections grinding led to samples of 100 to 200 µm thickness. Diamond pastes of 0.25 and 0.1 µm particle size were applied on felt disc to produce a smooth surface, using a polishing machine (Escil, France). The samples were finally cleaned ultrasonically to remove all remains. Both longitudinal and cross sections were prepared. The sections were glued to glass microscope slides using a transparent adhesive insoluble in acetone (Action-2510837), deplastified in acetone (Thermofisher scientific-AX0120) to remove the inclusion resin and rehydrated as usual by passing through xylenes and descending series of alcohol. After labeling the slides, the sections were ready to be processed and analyzed by optical microscopy, Raman microscopy and scanning electron microscopy. A classical histology scheme of rat tail vertebrae is represented in Figure 1.

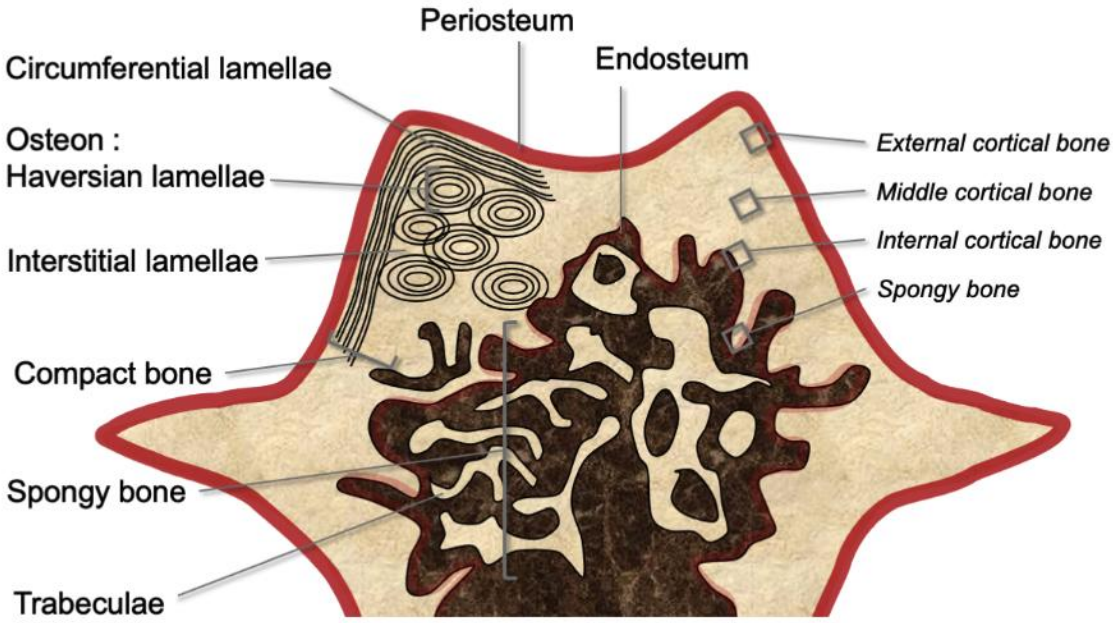

Figure 1. Illustrative scheme of transverse section of rat tail vertebrae. The zones where scans were performed are indicated.

2.2 Micro tomography

Rat vertebra was placed in an EasyTom 150 kV micro computed tomography (µCT) with an Xact software interface (RX Solution, Chavanod, France). The whole vertebra was placed in the hold sample, in the air. A 1 mm aluminum filter was placed in front of the X-ray source. The voltage used was 71 kV, with an intensity of 70 µA and a tube power of 4.68 W. To increase the signal-to-noise ratio, 4 images were recorded and averaged, and the gain reached 5, with an angular step of 0.25 degrees. A total of 2880 radiography-type images were collected over approximately one hour, and the reconstruction algorithm was performed by X-act software. Scanning time was around 30 minutes. A total of 2150 16-bit Tiff images were reconstructed in gray shades, with a voxel size of 5.9 µm. Ring artifacts and beam hardening corrections were not used here to avoid loss of information. Two dimensions data visualization, threshold and 3D reconstruction were performed with Fiji. Reconstructed meshes are visualized in Meshlab.

2.3 Confocal Raman microscopy

The area scans (see Figure 1) and single spectrum (spot scans) were performed on the commercial Witec Confocal Raman Microscope System alpha 300R (Witec Inc., Ulm,

Germany). The incident laser, with excitation assured by a 532 nm wavelength frequency doubled Nd: YAG (Newport, Evry, France), having a beam focused onto the sample through a ×20 and 0.4 numerical aperture objective (Nikon, Tokyo, Japan). With such objective, resolution of the system reaches 800 nm. The scans were performed on a square area of around 110x110 micrometers. Each area was scanned by 150 x150 points, each point corresponding to a spectrum. Area scan was done with an integration time of 0.2 second, to combine a good signal on noise ratio and a reasonable time scan. Each scan is between 1:45 and 2:00. Line scans were performed with 2 seconds integration time, with 5 spectra recorded and averaged, with 15 points on each line. To avoid outlier values, Cosmic Ray Removal (CRR) plugins was used.

2.4 Treatment of Raman data

Raman based images were reconstructed using a sum filter: a peak of interest was selected; for each point of the scanned zone area under the peak was measured. Using look up tables, each value could be connected to a hue and used to reconstruct a chemical mapping intensity. 960 cm^{-1} Phosphate peak intensity, 1660 cm^{-1} Amide I and 2950 cm^{-1} CH peak intensity were reconstructed for each sample. Also, the ratio image between 960 cm^{-1} and 1660 cm^{-1} peak intensity was reconstructed. K-mean cluster analysis was performed with Witec project 5.2 software. K-mean cluster analysis can be used to create an arbitrary number of groups of spectra, based on proximity/similarity. User choose the number of clusters to find division of image in the zone connected to phase, and centroid spectra of each zone is extracted. Using the software Spectragryph v1.2.15, spectra were cropped in the region of interest, from 400 to 3200 cm^{-1}. To eliminate background fluorescence, we used the adaptive algorithm, with a coarseness of 10%. To measure the ratio between peaks to avoid artifacts due to surface roughness or laser state, we normalized spectra with the most intense peak (Phosphate PO_4^{3-}) to compare relative intensity. Principal component analysis (PCA) and clustering was performed in the FactoMineR plugin in R v. 4.1.0 software. The PCA and the clustering test was not done on the whole spectra, but on the relative intensity of the peak.

2.5 Backscatter electron microscopy and Energy Dispersive Spectroscopy

Backscatter electron microscopy analysis was done with secondary electron images. Scans were performed with Analytic FEI Quanta FEG 200 microscope (MEA, University of Montpellier, France). Acceleration voltage was 15 kV, working distance 10 mm, and pressure was 45 e10−1 Torr. Sample coating was not required for Low Vacuum mode.

Energy Dispersive Spectroscopy was performed with Oxford Instruments Ultim Max 100 mm^2 (MEA, University of Montpellier, France) provided the chemical composition of bone in each part where Raman scans were done. In the external, central, internal cortical and spongy bone, 3 spectra were recorded each time.

2.6 Histology

Undecalcified vertebrae ground sections were stained with Weigert's haematoxylin in combination with light green and Orange G to visualize the arrangement of the bone canals in relation to various components of the bone and the periosteum (Gruber et al., 2002).

The samples were prepared, embedded, cut, mounted, deplastified and rehydrated as described above. Slides were first stained progressively with a fresh and filtered mixture of ferric-ammonium sulfate modified Wiegert's hematoxylin for five to ten minutes until the slides were well stained. Slides were rinsed in Scott's tap water initially for thirty seconds and then washed abundantly in tap water for two to three minutes to remove any gross deposits of the nuclear stain.

Orange-G staining was used in order to observe bone components orientation and the haversian system organization, with the following protocol: staining with freshly made Orange-G was processed for five to seven minutes. The free stain was rinsed off the slide with one percent acetic acid solution before washing in tap water for two to three minutes.

Light Green staining was used for an overall view of the haversian system with the following protocol: staining with light green was processed for forty minutes. The slides were then rinsed with acid alcohol and washed with tap water to remove the excess stain.

After staining, the samples were quickly dehydrated in xylene and mounted using a methacrylic acid based mounting medium (Eukit, Sigma Aldrich). The slides were let dry until the polymerization of the mounting medium.

3 Results

3.1 Characterization of osteonic canals by histology and microcomputed tomography

Osteonic canals formed a network of vessels and nerves and such microstructure could be studied with several techniques at different scale and resolution. To visualize the osteonic canals in rat vertebrae, we first performed classical histological stainings. After staining with hematoxylin/orange G (Figure 2A), the boundaries of the bone can be clearly seen as the periosteum whereas endosteum staining was more intense. The crystalline bone region was

less stained and remained clear. This allowed the visualization of the osteonic canals and the osteocytes within the relatively clearer bone mass, as they retained better the stain. The portions of the osteonic canals that project to the cut surface of the bone sample show a darker hue due to the direct visualization of the lumen of the canal emerging to the surface. A similar organization can be observed in the sample stained with hematoxylin/light green but with a more profound view of the branching in the canal system (Figure 2B).

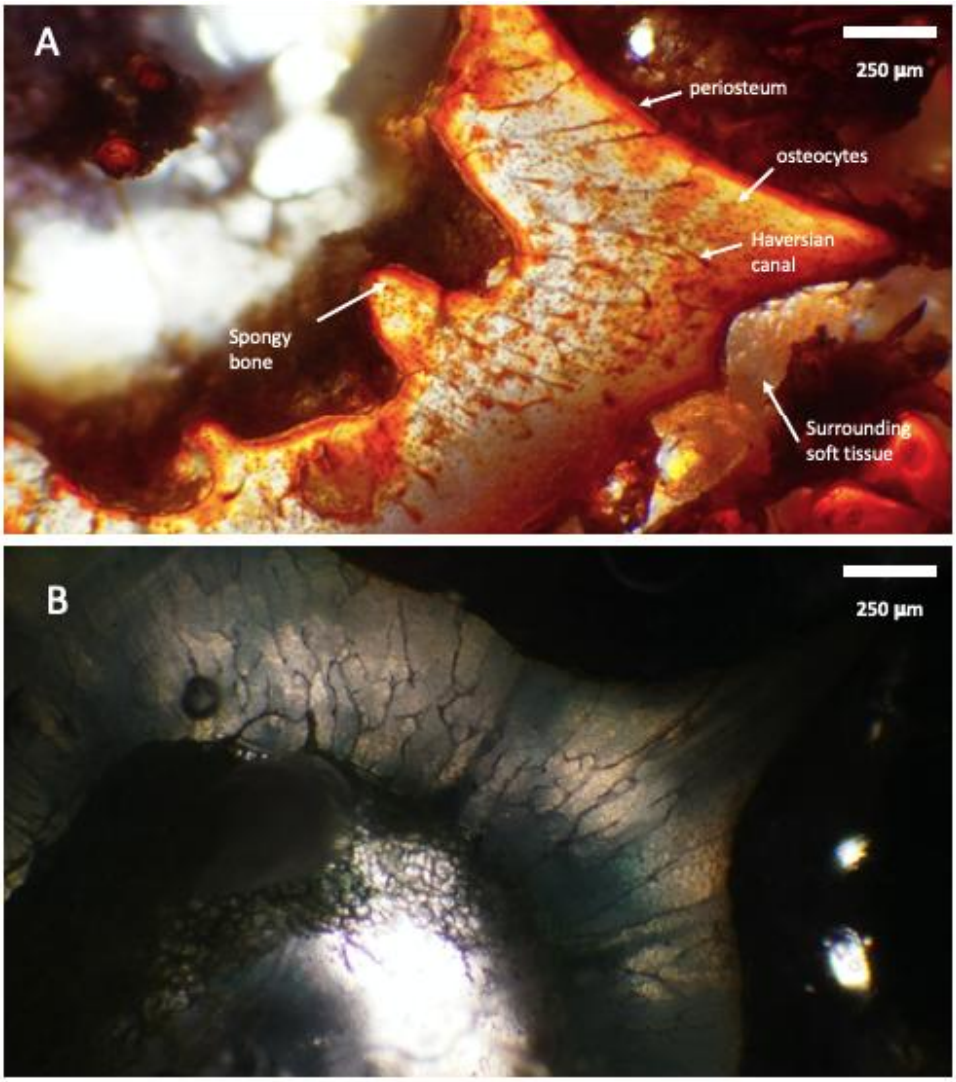

Figure 2. Classic histological staining with hematoxylin/orange G (A) and hematoxylin/light green plus (B).

In order to characterize the osteonic canals network, we used high resolution X-ray µCT. Figure 3 shows µCT grayscale image extracted from µCT scan and a 3D reconstruction from thresholding the air/bone interface. In Figure 3A, a transversal plane of vertebrae grayscale image is shown. Measures of mineral density realized on cortical and spongy bone, based on 8 bits grey shade values (after conversion) on 5 representative slices, for the mineral gave

very similar results, without any statistical difference: 170 (SD 12.2) for internal bone 173 (SD 13) for external bone.

The images extracted from the µCT scan showed the presence of osteonic canals, as expected with such resolution. Unlike the usual description of osteonic canals system is not parallel to the vertebra axis, but all canals are originating from the periosteum, at the external cortical part, and are progressing toward the internal cortical bone. All canals had an opening at the periosteal surface, and, in the cortical bone, these canals were observed as forming a front or a wave (red dash lines in Figure 3A). In some areas, two levels could even be observed, like parallel sheet of canals. Secondly, the high density of canals in specific zones appeared connected with diffuse regions of high mineralization. This is clearly visible on Figure 3B (red arrows).

Interestingly, the canals appeared orientated in a particular direction: in the whole vertebrae, canals exhibited an angulation from the surface of the bone in the direction of the spongy bone, as shown in Figure 3D. In the first approximation, canals seem directed in the center of the vertebrae and therefore, the canals localized in the caudal part were more oriented in the cranial direction and vice versa. Canals localized in the center of vertebrae are more perpendicular to the surface of the bone. For a more complete view of grayscale stack images extracted from µCT, see also supplementary Fig 1A and B.

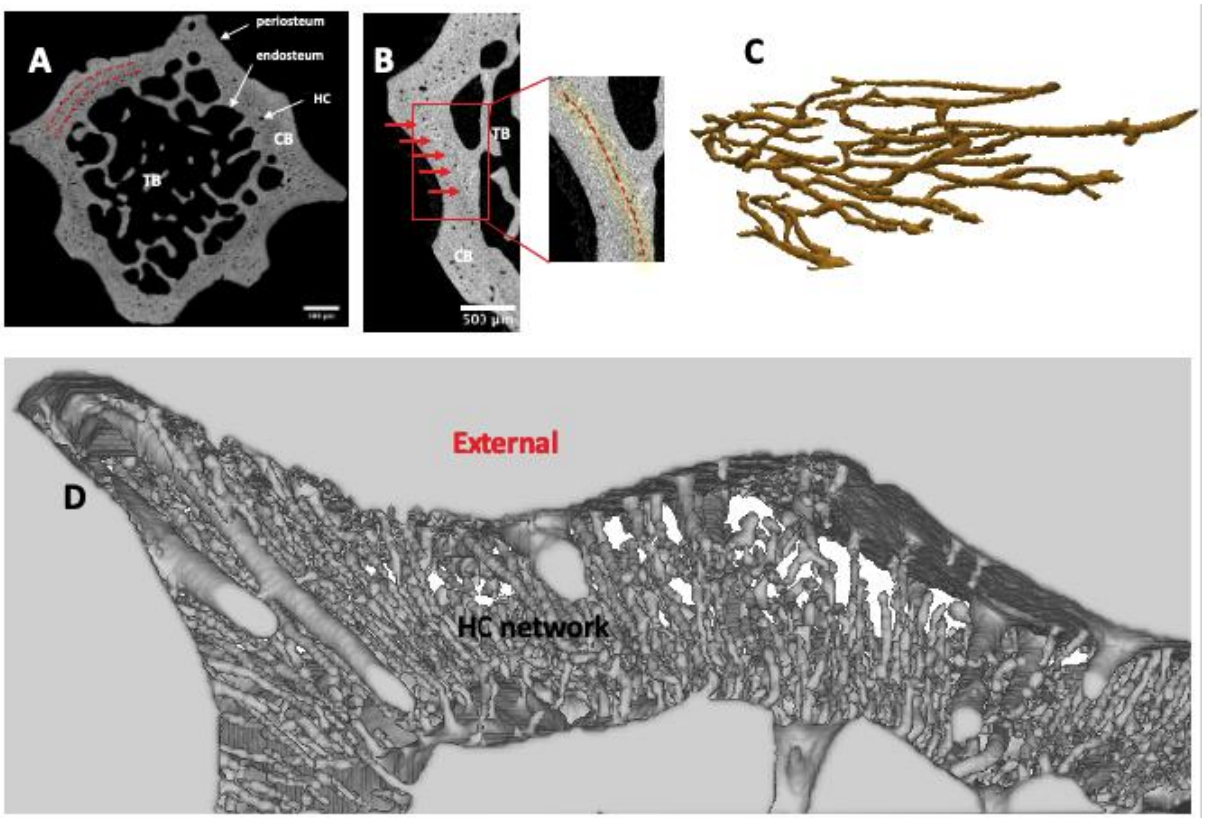

Figure 3. A) Grey shade µCT image of rat vertebra in transverse plane. B) cortical rat bone detail, red arrows indicate front line of haversian canals and bright zone connected to higher density; C) 3D view reconstructed of osteonic canals on cortical bone. D) 3D reconstruction of haversian canals network;

Moreover, the 3D pattern of osteonic canals was far from those presented in the usual histology scheme. Indeed, the size of canals are not homogeneous, as presented in Figure 4 and Table I. For information, in addition to canals parameters, cortical thickness in region where measures were done is 439.4 µm (SD 97.8 µm), and the surface of the cortical in sagittal plane is 5.13 mm^2 (SD 0.07 mm^2). Very few of the canals, which are not foramen, are bigger than others, and reach 80 µm in diameter. For more transversal plane images extracted of micro-CT, from caudal to cranial, see also Supplementary Fig 1. Figure 4 shows the diversity in size of canals collected in 5 representatives reconstructed 2D slice of vertebra. In all the images, the canals surfaces are in the range of 1.9 and 2.3% of the bone surface. Then, the classical distinction between Havers and Volkman canals is not so clear. The 3D network is more than entangled canals, with a preferred direction and connections and divergences, creating some branches, as illustrated in Figure 3D.

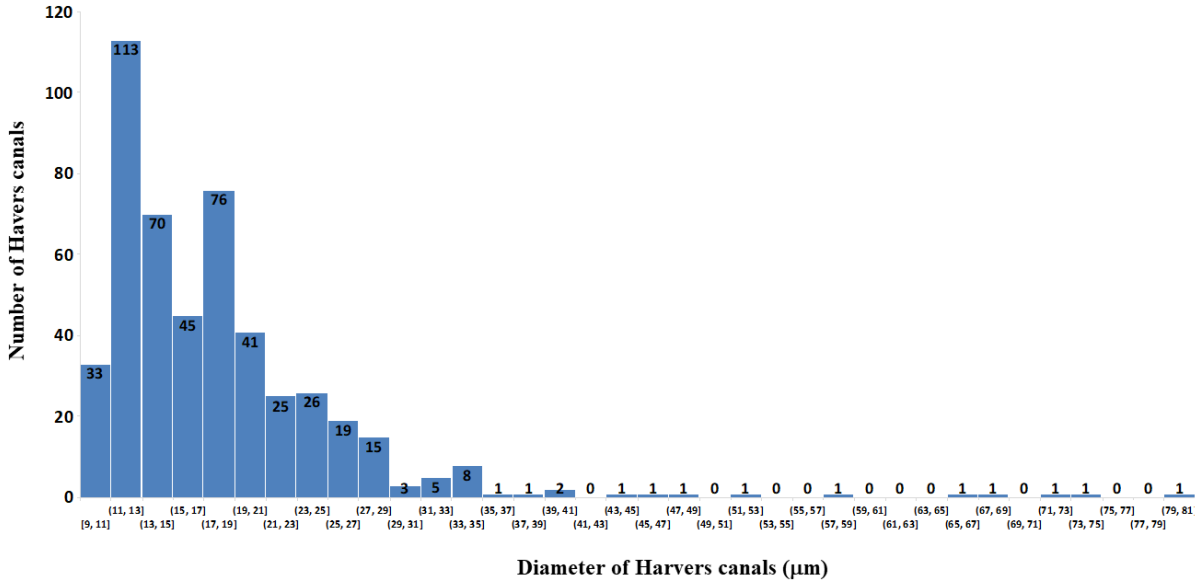

Figure 4. Distribution of Havers canals diameter.

Table I. Canals measurements done on (a) 5 representative gray shade slices (b) or on 45 canals (b) located in the three regions of the cortical bone (caudal, cranial and central).

	Mean (SD)	**Units**
Canal surface[a]	0.36 (0.01)	mm^2
Canal diameter[a]	18.4 (8.6)	µm
Canal density[a]	46.0 (9.9)	mm^{-2}
Canal length[b]	450.0 (152)	µm

3.2 Comparison of the different regions of the cortical bone

In order to characterize the different regions of the rat vertebrae cortical bone, a frontal slice of the first caudal vertebra was prepared, and many zones were scanned by using backscatter electron imaging. Images were taken in the external, central and internal cortical bone, and in the spongy bone. The different zones are presented in Figure 5. These images show lamellar bone in external and internal part of cortical bone. Osteocytes are present in all parts of scanned area. In the central part of the cortical bone (Figure 5B), differences in greyscale reveal heterogeneities in bone mineralization. This result could be connected to micro-CT images, where cortical bone appeared with difference in mineral density (Figure 3B).

Energy Dispersive Spectroscopy results (supplementary table I) showed a singularity about spongy bone spectra. Indeed, mean carbon atomic concentration was evaluated to 64% in trabecular bone and only to 24% in cortical bone. On the contrary, the oxygen atomic rate was 37 % in trabecular bone and 40% in cortical bone.

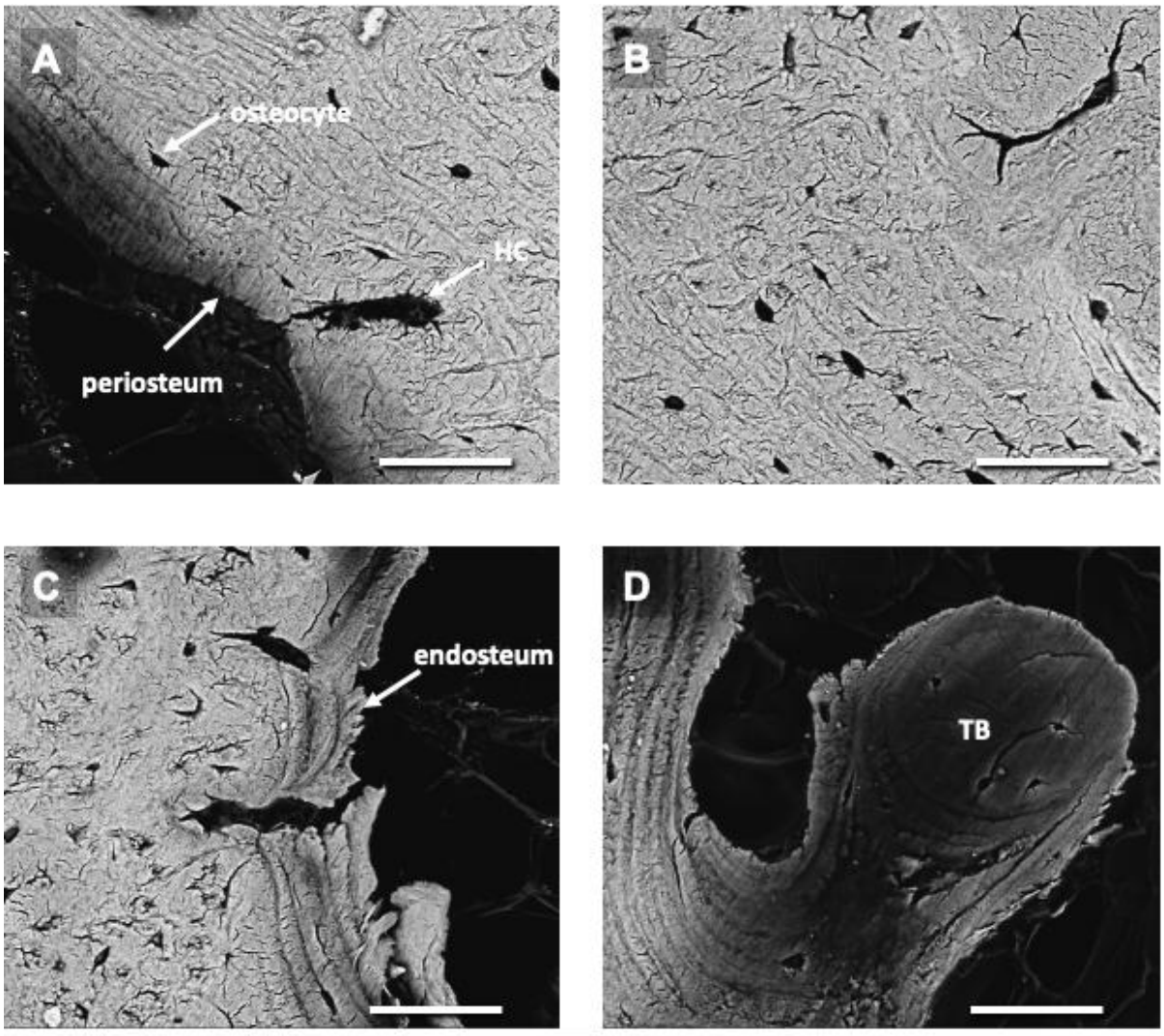

Figure 5. Scanning electron microscopy images. A) external, B) central, C) internal cortical bone and D) trabecular bone. Scale bar: 50 µm.

We then used confocal Raman microscopy of the same zones of the cortical bone to establish particulate hydroxyapatite and protein composition in the external, in the bulk/central, and in the internal part of the bone. To evaluate the first approximation difference visible between each part of vertebrae rat bone, we used long time integration spectra. Indeed, a long integration time in single spectra increases the signal-to-noise ratio. Representative spectra of the four scanned zones are plotted in Figure 6, with labeling of some of the peaks. In these

spectra, with peaks in the same wavenumber, signature of hydroxyapatite is clearly visible, in particular with stretching mode of PO_4^{3-} vibration and carbonate. The CH and amide are important components, due to the presence of protein and collagen. All the peaks are at the same wavenumber and no shift could be measured.

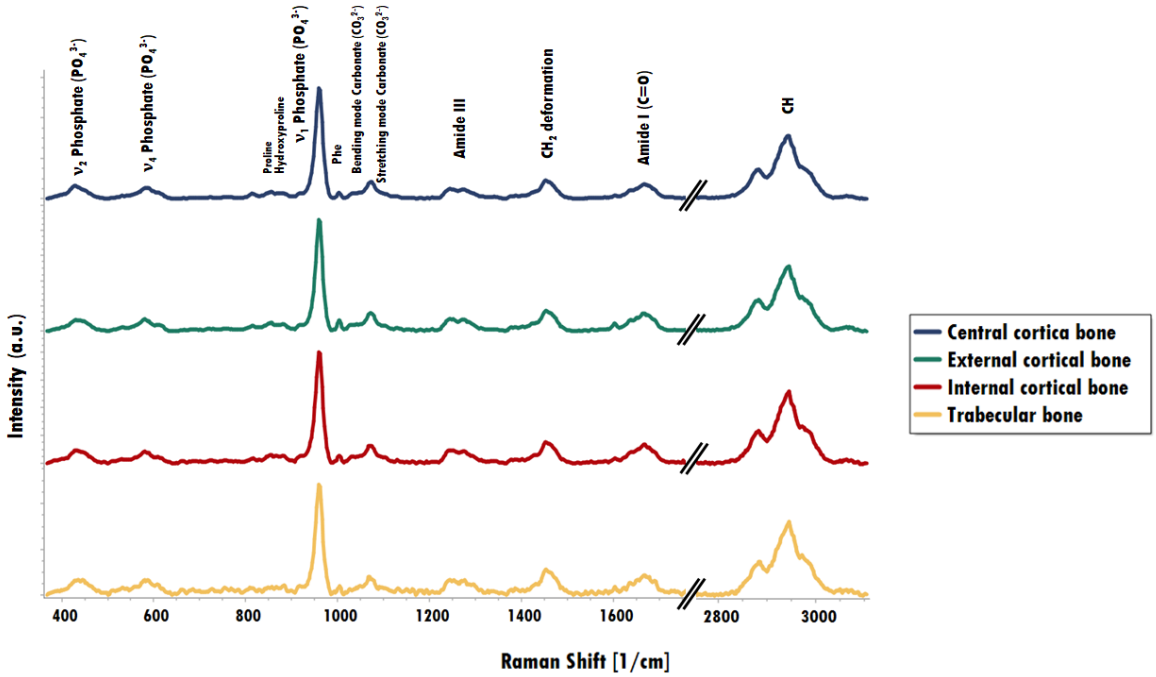

Figure 6. Characteristic Raman spectra for the 4 scanned areas: external, central, internal cortical bone, and trabecular bone.

Figure 7 shows images reconstructed with area integration of phosphate, amide and CH peak. Every known structure could be observed with a difference in chemical composition: osteocyte, havers canal, lamellar bone, difference in density or in protein content. Contrast of structure could be increased in selecting a specific peak intensity reconstruction, *i.e* lamellar pattern in external cortical bone. Each cartography reveals variations of Phosphate, Amide I and protein with 960 cm^{-1}, 1660 cm^{-1} and 2950 cm^{-1} peak intensity respectively. In these results, lamellar bone, osteon, osteocytes and Havers canals are clearly visible. Dynamics are

more pronounced in protein images, indicating a higher contrast in Raman microscopy.

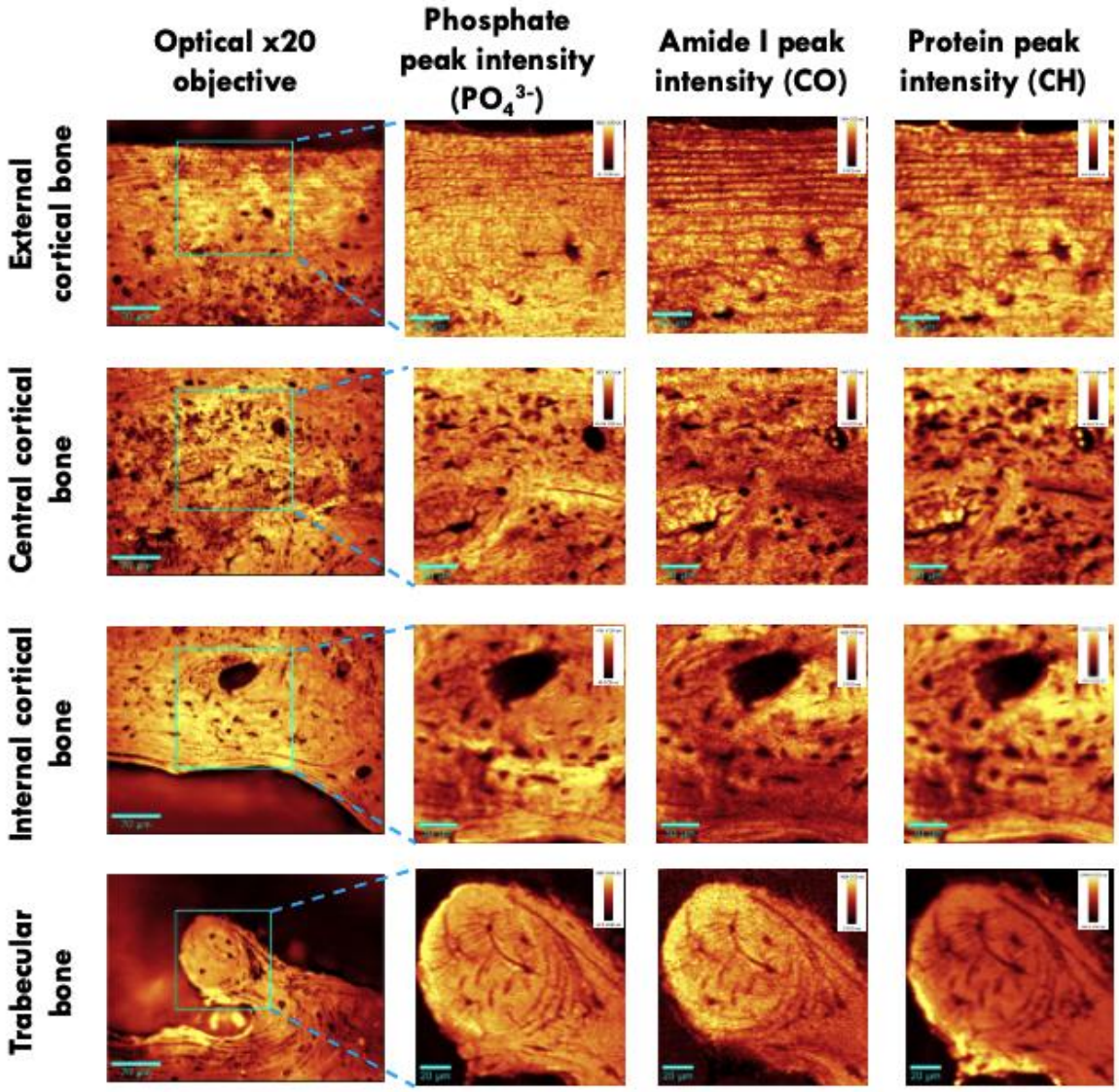

Figure 7. Image reconstructed with Raman spectra. from the top to the bottom: external, central, internal cortical bone and trabecular bone. First column: optical image x20; second column: 960 cm^{-1} Phosphate peak intensity mapping; third column: 1660 cm^{-1} amide I peak intensity mapping; forth column: 2950 cm^{-1} CH peak intensity mapping

Table II shows ratio peak intensity with statistical analysis. One can notice that significant differences are detected in the tree area probed, and every ratio, even when they are close, such as CO_3 to ν_1 and ν_2 PO4, give different statistical results.

Table II. Raman peak intensity ratio in the four parts of vertebrae rat bone

Compound ratio	**ν_1 PO_4 to amide I ratio (mineral to collagen)**	**ν_2 PO_4 to amide III ratio (mineral to collagen)**	**CO_3 to ν_1 PO_4 ratio (carbonate to phosphate)**	**CO_3 to ν_2 PO_4 ratio (carbonate to phosphate)**
Wavenumber of compound	960/1660	430/1246	1070/960	1070/430
Supposed connection	*Lamellar bone orientation*	*Variation in bone*	*Variation in bone*	*Variation in bone*
External cortical	3.92 (SD 0.43)^{c,i,t}	0.76 (SD 0.09)^{c,i,t}	0.23 (SD 0.02)	1.41 (SD 0.14)^{c}
Central cortical	5.65 (SD 0,58)^{e}	0.89 (SD 0,05)^{e}	0.22 (SD 0,01)	1.58 (SD 0,11)^{e}
Internal cortical	5.27 (SD 0.38)^{e}	0.82 (SD 0.04)^{e}	0.20 (SD 0.02)	1.37 (SD 0.11)
Trabecular	5.26 (SD 0.33)^{e}	0.83 (SD 0.07)^{e}	0.20 (SD 0.01)	1.47 (SD 0.08)

Superscripts indicate whether there was a significant difference ($p<0.05$); e: external; c: central; i: internal; t: trabecular.

With the same spectra collected for ratio comparison, PCA was performed, and results are shown in Figure 8. To complete these results, the K-mean clustering was done to compare cloud points and the 4 clusters. Statistical analysis, with one way ANOVA or PCA, gave interesting results, enabling us to distinguish different kinds of bone, depending on which ratio is compared. For example, external and central could not be seen significantly different with phosphate to amide I and III or carbonate to Phosphate ratio, but have been tested successfully with carbonate to ν_2 Phosphate ratio (see table II). Each group of spectra has a specific ratio which presents a significant difference. In Figure 8, the global difference on the two first axes, represents 74% of the variability of the spectra, the external and central part of cortical bone could not be distinguished. This is confirmed by the hierarchical clustering test, where 4 clusters have been chosen, but the central and external zone were merged together.

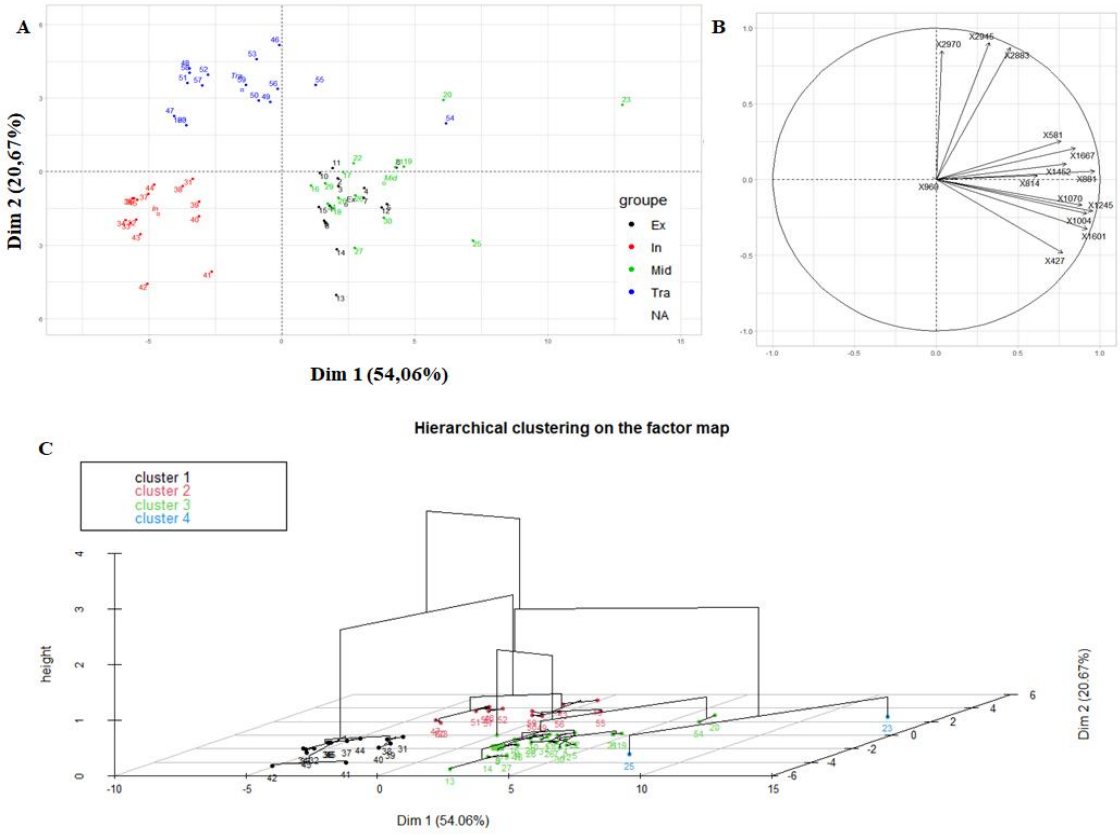

Figure 8. PCA analysis of the four groups of spectra recorded in external (Ex), central (Mid) and internal (Int) cortical bone and trabecular bone (Tra). A) first and second principal axis ; B) correlation circle, where each variable could be connected to an axis seen in A; C) tree representation of 4 k-mean clusters.

3.3 Characterization of the lamellar bone

In the rat vertebra, the presence of lamellar bone was observed in the 100 micrometers external part of the cortical bone. A same layer pattern was observed in a relatively smaller zone (around 20 micrometers) of the internal region of the cortical bone. These alternative bands were seen with Phosphate intensity and CH_2 deformation peak. These lamellar patterns were more clearly visible with the Phosphate to Amide 1 (960/1660 cm^{-1}) ratio reconstructed image (Figure 9A). On the external bone, bone lamellae correspond to bright and dark layers in Raman, with an increasing width, from 4.5 µm in the most external area, to 10/20 µm in the inner part of the scanned zone (Figure 9B).

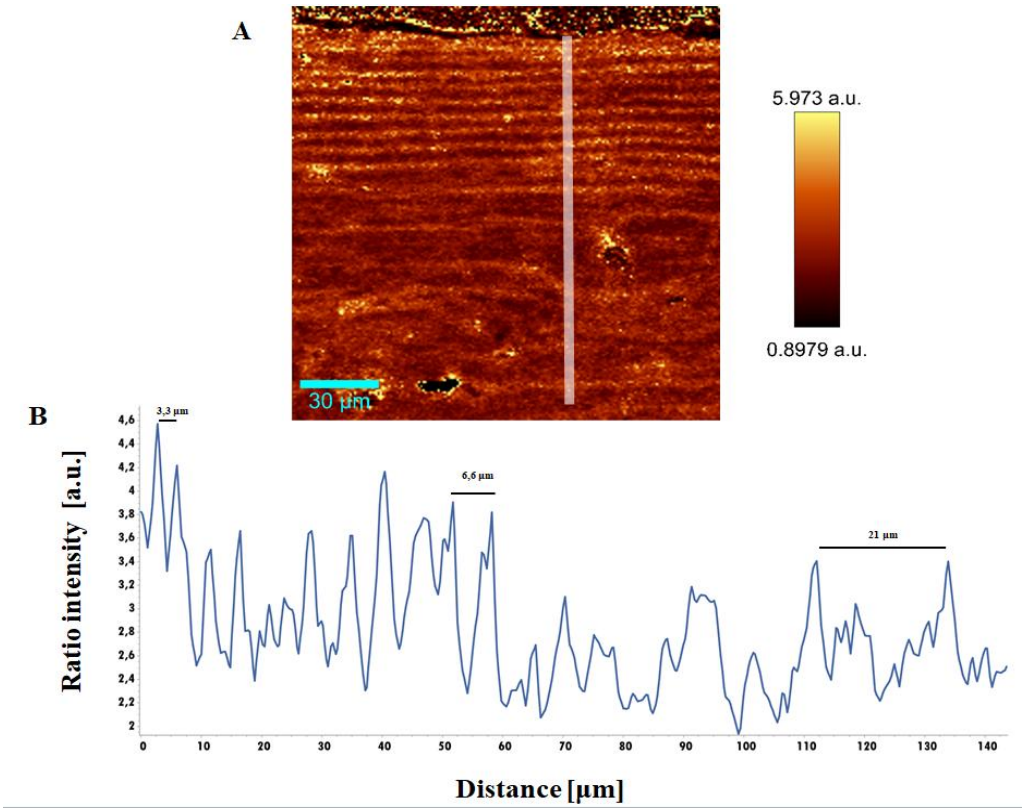

Figure 9. 960/1660 cm^{-1} Raman intensity peak ratio. A) cartography of ratio with connected lookup table. B) plotted profile corresponding to the line shown in A.

Circular lamellae around osteon were also revealed by Backscatter electron microscopy (Figure 10) and by Raman imaging, as shown in Figure 11. Backscatter electron microscopy image (Figure 10 A) was noisier compared to Raman peak intensity (Figure 11B-D). Several images were reconstructed with selection of different peaks shown in Figure 6. Then, images ratio could be reconstructed by division of two images (Figure 11E-G). Enlargement of circular lamellae around osteon have been evaluated from a plotted profile of carbonate on ν_1 phosphate images (Figure 11H). From around 4.7 µm close to the center, the distance between two phosphate-enriched lamellae reached to around 7 µm.

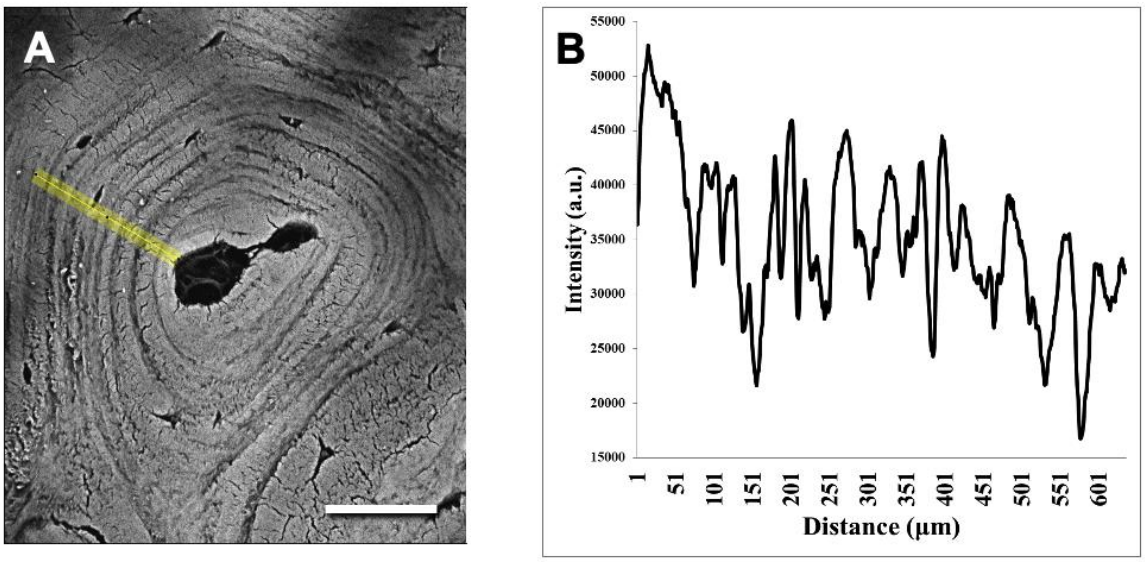

Figure 10. Scanning electron microscopy image of the lamellar bone around an osteon. In panel B, a plotted of intensity is represented to illustrate formation of bone in concentric circles, and measurement of spatial frequencies could be evaluated. Scale bar: 50 µm.

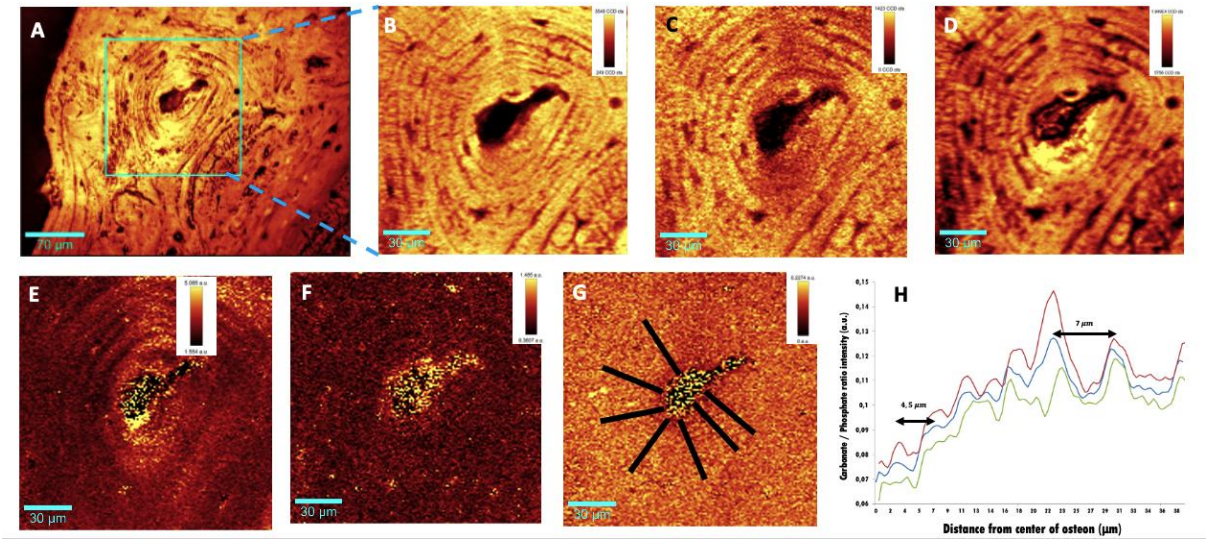

Figure 11. A) optical image x20; B) 960 cm^{-1}; C) 1660 cm^{-1}; D 2950 cm^{-1}; E) Ratio phosphate 960/amide I 1660; F) Ratio phosphate 430/amide III 1246; G) Ratio carbonate/ν_1 phosphate; H) plotted profile of black line shown in G (blue line: mean curve; red and green line: standard deviation curves).

4 Discussion

In this study, we have combined chemical imaging by confocal Raman microscopy with Backscatter electron microscopy and high resolution micro-computed tomography in order to precise the 3D microstructure of the cortical bone of the rat vertebrae. Thus, we were able to provide data on the composition of the external, central, and internal part of the cortical bone and on the dynamic of the network of HC. With all these results, a quite complete representation of this type bone at different scale is exposed, with the particularities of rat tail microstructure.

The different techniques can be used as complementary information to precisely describe bone quality, with a specific interest to assess newly formed bone in case of bone regeneration therapies. The main characteristics of these techniques are summarized in Table III.

Table III: summary table of technics used to characterize rat bone vertebrae

	Size of ROI	**Time for sample preparation**	**Time for imaging**	**Material Cost**	**Single manip cost**	**Resolution**	**Structure seen**	**Interest**	**Difficulty**
Confocal Raman microscopy	*~150 um (depending pizeo table)*	*5 days min*	*Around 1 hour*	*Expensive*	*Cheap*	*1um/300nm depending microscope objective*	*Osteocyte, lamella bone, osteonic canals*	*Chemical mapping, spectral analysis*	*Difficult*
SEM	*10mm to 10 um*	*5 days min*	*Few minutes*	*Expensive*	*Cheap*	*100 um to few nm*	*Osteocyte, lamella bone, osteonic canals*	*High resolution*	*Moderate*
Micro CT	*2*2*2cm^3 (whole vertebrae)*	*0*	*30 minutes*	*Expensive*	*Cheap*	*2 to 5 micrometers, depending X ray source*	*3D internal structure as spongy bone and osteocyte network*	*3D internal structure, non destructive, without preparation*	*Easy*
Classical histology	*5*5mm^2*	*5 days min*	*instantaneous*	*Cheap*	*Cheap*	*1um/300nm depending microscope objective*	*Osteocyte, lamella bone, osteonic canals*	*Easy, several coloration protocols*	*Moderate*

Using Raman spectra coupled to Backscatter electron microscopy and Energy Dispersive Spectroscopy, significant differences in bone composition were observed. In particular, difference in grey shade can be noted in central part of the cortical bone. This is the consequence of neoformed (darkest hue) and older bone (brightest hue), as already observed in a previous study with electron microscopy on healthy human bone (Ruffoni et al., 2007). With a lower resolution, micro tomography images showed similar variation in bone density (Figure 2B). Energy Dispersive Spectroscopy results showed a singularity about spongy bone

spectra with differences in Carbon and Oxygen concentration as compared to cortical bone. Even though this observation cannot be fully explained, such a difference between these two main kinds of bone had not been previously reported in literature. Further exploration will be required to confirm or infirm this first observation. If previous Raman analysis have compared old and young bone in femur mice, in different planes (Gamsjaeger et al., 2010), the present study is the first comparative analysis using Raman confocal microscopy of cortical and spongy bone.

Our PCA clustering analysis from Raman peaks intensity showed that inner and external cortical bone could be distinguished from trabecular bone and from the central zone of the cortical bone, although the two later cannot be separated one from each other. This observation indicates (1) a difference in the chemical composition between central and external cortical on one hand, and inner cortical and trabecular bone on the other hand, and (2) a difference of composition between trabecular and inner part of cortical. This is confirmed by statistical difference found in peaks intensity ratio, as shown in table II. The combination of global analysis with PCA would benefit to be completed with ANOVA to find a ratio that could distinguish the four considered regions.

In the whole rat vertebra, canals are oriented from the surface of the bone towards the center of the vertebra with an angulation between canals and surface. Consequently, the canals localized in the caudal part are more oriented in the cranial direction and vice versa. Canals localized in the center of vertebrae are more perpendicular to the surface of the bone. This could be seen in supplementary Fig 1B. Surprisingly, the 3D pattern of Havers canals is far from those presented in the usual histology scheme. Indeed, the size of canals were not homogeneous, as presented in Figure 8 and Table II. These results are far from previously published studies about orientation of osteonic canals in bone. Indeed, in µCT femur 3D meshes, osteonic canals were clearly oriented parallel to the long bone axis (Cooper et al., 2003), while rat vertebrae show an orientation of all the osteonic canals in the direction of the center of the vertebrae. In another investigation on rat cortical bone (femur), the 3D reconstruction did not allow to conclude anything about the whole dynamic of the osteonic canals network, as the reconstruction was done from histology slices, leading to too small volumes (Kim et al., 2015).

However, some of our results about osteonic canals, such as diameter, number, density, will have to be confirmed by other experiments, because of some limitation of our experimental setup. Indeed, the micro tomography used presents a good resolution, but some canals have a

size close to this limit. Thus, the density could actually be higher, and the average diameter lower.

Finally, circular lamellae around osteon were also revealed by Backscatter electron microscopy (Figure 9) and by Raman imaging, as shown in Figure 10. Variation in orientation of such collagen fibril around osteonic canals had been previously described by Raman microscopy analysis (Schrof et al., 2014), but enlargement of such layer in circumferential lamellar had never been described. It remains unclear if the peripheral lamellar bone and the lamellar bone around the osteons are connected and originating from the same period of formation, or if they are independent. Indeed, from µCT images, the osteonic channels forms a tangle and cross the cortical region from one side to the other. Therefore, we hypothesize that the peripheral lamellar bone may invaginate towards the center of the vertebra, following the osteonic channels. Further investigation will be required, focusing on the connection between these two types of lamellae.

5 Conclusions

By combining several techniques, with different scale and kind of images, chemical, 3D, high resolution, quantitative, this study provides for the first time an in-depth analysis of the rat vertebrae cortical bone. The rat vertebral bone is chemically quite similar to human bone. The chemical composition of the cortical bone, whose Raman spectra were analyzed by PCA, seems to be indistinguishable between the outer and the central area, but has significant differences with the inner part and the cancellous bone. However, it has its own architecture, which differs from the structures found in human bone. The network of Havers canals is dense and oriented towards the center of the vertebra. Enlargement of layer size in circumferential lamellar and osteonic canals lamellar bone is observed and could be measure with Raman image.

Chemical analysis with Raman spectra highlighted differences in bone composition between external, central, internal cortical bone with significant differences in the CO_3 to ν_2 PO_4 ratio. Micro-CT imaging of the cortical bone revealed a dense and complex network of osteonic canals, starting to the surface in the direction of the center of the vertebrae. Using confocal Raman microscopy, we clearly observed an enlargement of bone lamellae layer around osteonic canals. Altogether, this work is the first in-depth characterization of the rat vertebrae

cortical bone microstructure. This description is a necessary step for a complete animal model, which will allow the analysis of bone regeneration in the future.

Acknowledgments

Authors thank Renaud Lebrun (Institut des Sciences de l'Evolution de Montpellier – ISEM, Univ. Montpellier, CNRS) for his assistance in microtomography data acquisition. 3D data acquisitions were performed using the micro-CT facilities of the MRI platform member of the national infrastructure France-BioImaging supported by the French National Research Agency (ANR-10-INBS-04, « Investments for the future »), and of the Labex CEMEB (ANR-10-LABX-0004) and NUMEV (ANR-10-LABX-0020). Thanks to Maxime Bedez for his expertise in back scattered mode of scanning electron microscopy on bone.

Research data.

Micro tomography raw data are downloadable at:
https://data.mendeley.com/datasets/xtdrxjxccv/draft?a=83f567fb-11f4-42e7-8844-b302b8fb3abb

Raman raw data are downloadable at:
https://data.mendeley.com/datasets/f6t82979np/draft?a=d656e7ad-7687-4721-8b55-f5166cb0c014

SEM/EDX raw data are downloadable at:
https://data.mendeley.com/datasets/5j22kfstnp/draft?a=f5e8870b-48ce-4867-ab23-096d49bbb107

References

Adachi, T., Boschetto, F., Miyamoto, N., Yamamoto, T., Marin, E., Zhu, W., Kanamura, N., Tahara, Y., Akiyoshi, K., Mazda, O., Nishimura, I., & Pezzotti, G. (2020). In Vivo Regeneration of Large Bone Defects by Cross-Linked Porous Hydrogel : A Pilot Study in Mice Combining Micro Tomography, Histological Analyses, Raman Spectroscopy and Synchrotron Infrared Imaging. *Materials*, *13*(19), 4275. https://doi.org/10.3390/ma13194275

Akkus, O., Adar, F., & Schaffler, M. B. (2004). Age-related changes in physicochemical properties of mineral crystals are related to impaired mechanical function of cortical bone. *Bone*, *34*(3), 443‐453.

Awonusi, A., Morris, M. D., & Tecklenburg, M. M. (2007). Carbonate assignment and calibration in the Raman spectrum of apatite. *Calcified tissue international*, *81*(1), 46‐52.

Belaid, H., Barou, C., Collart-Dutilleul, P.-Y., Desoutter, A., Kajdan, M., Bernex, F., Tétreau, R., Cuisinier, F., Barés, J., & Huon, V. (2022). Fabrication of Radio-Opaque and Macroporous Injectable Calcium Phosphate Cement. *ACS Applied Bio Materials*, *5*(6), 3075‐3085.

Blazsek, J., Dobó Nagy, C., Blazsek, I., Varga, R., Vecsei, B., Fejérdy, P., & Varga, G. (2009). Aminobisphosphonate Stimulates Bone Regeneration and Enforces Consolidation of Titanium Implant into a New Rat Caudal Vertebrae Model. *Pathology & Oncology Research*, *15*(4), 567‐577. https://doi.org/10.1007/s12253-009-9156-y

Cooper, D. M., Turinsky, A. L., Sensen, C. W., & Hallgrímsson, B. (2003). Quantitative 3D analysis of the canal network in cortical bone by micro-computed tomography. *The Anatomical Record Part B: The New Anatomist: An Official Publication of the American Association of Anatomists*, *274*(1), 169‐179.

Freeman, J. J., Wopenka, B., Silva, M. J., & Pasteris, J. D. (2001). Raman spectroscopic detection of changes in bioapatite in mouse femora as a function of age and in vitro fluoride treatment. *Calcified tissue international*, *68*(3).

Frost, H. M., & Jee, W. S. (1992). On the rat model of human osteopenias and osteoporoses. *Bone and mineral*, *18*(3), 227‐236.

Gamsjaeger, S., Masic, A., Roschger, P., Kazanci, M., Dunlop, J. W. C., Klaushofer, K., Paschalis, E. P., & Fratzl, P. (2010). Cortical bone composition and orientation as a function of animal and tissue age in mice by Raman spectroscopy. *Bone*, *47*(2), 392‐399. https://doi.org/10.1016/j.bone.2010.04.608

Gatin, E. G., Nagy, P., Iordache, S.-M., Iordache, A.-M., & Luculescu, C. R. (2022). Raman Spectroscopy : In Vivo Application for Bone Evaluation in Oral Reconstructive (Regenerative) Surgery. *Diagnostics*, *12*(3), 723. https://doi.org/10.3390/diagnostics12030723

Goldberg, M., Kulkarni, A. B., Young, M., & Boskey, A. (2011). Dentin : Structure, Composition and Mineralization: The role of dentin ECM in dentin formation and mineralization. *Frontiers in bioscience (Elite edition)*, *3*, 711.

Gregor, T., Kochová, P., Eberlová, L., Nedorost, L., Prosecká, E., Liška, V., Mírka, H., Kachlík, D., Pirner, I., & Zimmermann, P. (2012). Correlating micro-CT imaging with quantitative histology. *Injury and skeletal biomechanics*, *10*, 48680.

Gruber, H. E., Ingram, J., & Hanley, E. N. (2002). An improved staining method for intervertebral disc tissue. *Biotechnic & Histochemistry: Official Publication of the Biological*

Stain Commission, *77*(2), 81‐83.

Hall, B. K. (2005). *Bones and cartilage : Developmental and evolutionary skeletal biology*. Elsevier.

Iwasaki, Y., Kazama, J. J., Yamato, H., & Fukagawa, M. (2011). Changes in chemical composition of cortical bone associated with bone fragility in rat model with chronic kidney disease. *Bone*, *48*(6), 1260‐1267.

Kazanci, M., Wagner, H. D., Manjubala, N. I., Gupta, H. S., Paschalis, E., Roschger, P., & Fratzl, P. (2007). Raman imaging of two orthogonal planes within cortical bone. *Bone*, *41*(3), 456‐461.

Khalid, M., Bora, T., Ghaithi, A. A., Thukral, S., & Dutta, J. (2018). Raman Spectroscopy detects changes in Bone Mineral Quality and Collagen Cross-linkage in Staphylococcus Infected Human Bone. *Scientific Reports*, *8*(1), 9417. https://doi.org/10.1038/s41598-018-27752-z

Kim, J.-N., Lee, J.-Y., Shin, K.-J., Gil, Y.-C., Koh, K.-S., & Song, W.-C. (2015). Haversian system of compact bone and comparison between endosteal and periosteal sides using three-dimensional reconstruction in rat. *Anatomy & Cell Biology*, *48*(4), 258‐261. https://doi.org/10.5115/acb.2015.48.4.258

Kubíková, T., Bartoš, M., Juhas, Š., Suchý, T., Sauerová, P., Hubálek-Kalbáčová, M., & Tonar, Z. (2018). Comparison of ground sections, paraffin sections and micro-CT imaging of bone from the epiphysis of the porcine femur for morphometric evaluation. *Annals of Anatomy-Anatomischer Anzeiger*, *220*, 85‐96.

Liu, D., Wagner, H. D., & Weiner, S. (2000). Bending and fracture of compact circumferential and osteonal lamellar bone of the baboon tibia. *Journal of Materials Science: Materials in Medicine*, *11*(1), 49‐60. https://doi.org/10.1023/A:1008989719560

Morris, M. D., & Mandair, G. S. (2011). Raman assessment of bone quality. *Clinical Orthopaedics and Related Research®*, *469*(8), 2160‐2169.

Moura, C. C., Tare, R. S., Oreffo, R. O. C., & Mahajan, S. (2016). Raman spectroscopy and coherent anti-Stokes Raman scattering imaging : Prospective tools for monitoring skeletal cells and skeletal regeneration. *Journal of The Royal Society Interface*, *13*(118), 20160182. https://doi.org/10.1098/rsif.2016.0182

Nieuwoudt, M. K., Shahlori, R., Naot, D., Patel, R., Holtkamp, H., Aguergaray, C., Watson, M., Musson, D., Brown, C., Dalbeth, N., Cornish, J., & Simpson, M. C. (2020). Raman spectroscopy reveals age- and sex-related differences in cortical bone from people with osteoarthritis. *Scientific Reports*, *10*(1), 19443. https://doi.org/10.1038/s41598-020-76337-2

Nyman, J. S., Makowski, A. J., Patil, C. A., Masui, T. P., O'Quinn, E. C., Bi, X., Guelcher, S. A., Nicollela, D. P., & Mahadevan-Jansen, A. (2011). Measuring Differences in Compositional Properties of Bone Tissue by Confocal Raman Spectroscopy. *Calcified Tissue International*, *89*(2), 111‐122. https://doi.org/10.1007/s00223-011-9497-x

Particelli, F., Mecozzi, L., Beraudi, A., Montesi, M., Baruffaldi, F., & Viceconti, M. (2012). A comparison between micro-CT and histology for the evaluation of cortical bone : Effect of polymethylmethacrylate embedding on structural parameters. *Journal of microscopy*, *245*(3), 302‐310.

Pearce, A. I., Richards, R. G., Milz, S., Schneider, E., & Pearce, S. G. (2007). Animal models for implant biomaterial research in bone : A review. *Eur Cell Mater*, *13*(1), 1‐10.

Pritchard, J. J. (1972). General histology of bone. *The biochemistry and physiology of bone*, *1*.

Raghavan, M., Sahar, N. D., Kohn, D. H., & Morris, M. D. (2012). Age-specific profiles of tissue-level composition and mechanical properties in murine cortical bone. *Bone*, *50*(4), 942‐953.

Renaud, M., Farkasdi, S., Pons, C., Panayotov, I., Collart-Dutilleul, P.-Y., Taillades, H., Desoutter, A., Bousquet, P., Varga, G., Cuisinier, F., & Yachouh, J. (2016). A New Rat Model for Translational Research in Bone Regeneration. *Tissue Engineering Part C: Methods*, *22*(2), 125‐131. https://doi.org/10.1089/ten.tec.2015.0187

Ruffoni, D., Fratzl, P., Roschger, P., Klaushofer, K., & Weinkamer, R. (2007). The bone mineralization density distribution as a fingerprint of the mineralization process. *Bone*, *40*(5), 1308‐1319. https://doi.org/10.1016/j.bone.2007.01.012

Schrof, S., Varga, P., Galvis, L., Raum, K., & Masic, A. (2014). 3D Raman mapping of the collagen fibril orientation in human osteonal lamellae. *Journal of Structural Biology*, *187*(3), 266‐275.

Shah, F. A. (2020). Towards refining Raman spectroscopy-based assessment of bone composition. *Scientific Reports*, *10*(1), 16662. https://doi.org/10.1038/s41598-020-73559-2

Sheyn, D., Kallai, I., Tawackoli, W., Cohn Yakubovich, D., Oh, A., Su, S., Da, X., Lavi, A., Kimelman-Bleich, N., & Zilberman, Y. (2011). Gene-modified adult stem cells regenerate vertebral bone defect in a rat model. *Molecular pharmaceutics*, *8*(5), 1592‐1601.

Unal, M., Ahmed, R., Mahadevan-Jansen, A., & Nyman, J. S. (2021). Compositional assessment of bone by Raman spectroscopy. *Analyst*, *146*(24), 7464‐7490. https://doi.org/10.1039/D1AN01560E

Viguet-Carrin, S., Garnero, P., & Delmas, P. D. (2006). The role of collagen in bone strength. *Osteoporosis international*, *17*(3), 319‐336.

Wang, M. L., Massie, J., Allen, R. T., Lee, Y.-P., & Kim, C. W. (2008). Altered bioreactivity and limited osteoconductivity of calcium sulfate–based bone cements in the osteoporotic rat spine. *The Spine Journal*, *8*(2), 340‐350. https://doi.org/10.1016/j.spinee.2007.06.003

Weber, B., Lackner, I., Haffner-Luntzer, M., Palmer, A., Pressmar, J., Scharffetter-Kochanek, K., Knöll, B., Schrezenemeier, H., Relja, B., & Kalbitz, M. (2019). Modeling trauma in rats : Similarities to humans and potential pitfalls to consider. *Journal of translational medicine*, *17*, 1‐19.

Weiner, S., Traub, W., & Wagner, H. D. (1999). Lamellar Bone : Structure–Function Relations. *Journal of Structural Biology*, *126*(3), 241‐255. https://doi.org/10.1006/jsbi.1999.4107

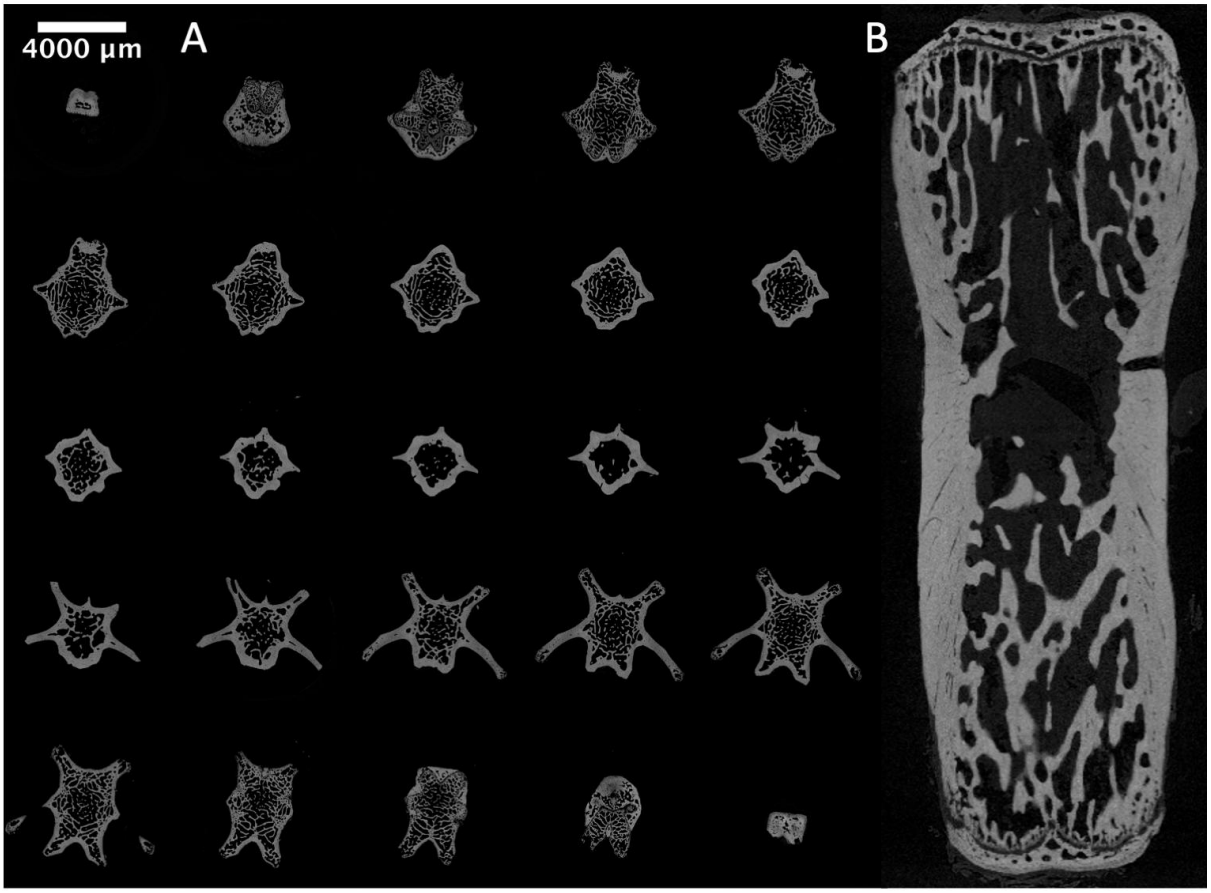

Supplementary Figure 1. A) Grey shade images montage extracted from the micro tomograph scan of the rat vertebra, from the caudal part (top left) to the cranial part (bottom right); B) Sagittal plane of the vertebra.

Supplementary Table I

Relative atomic and weight percentage of composition of external, central, internal and trabecular bone from Energy Dispersive Spectroscopy spectra analysis

	external bone		**middle bone**		**internal bone**		**trabecular bone**	
Spectrum Label	**Atomic %**	**weight %**	**Atomic %**	**weight %**	**Atomic %**	**weight %**	**Atomic %**	**weight %**
C	37.9	25.0	36.7	23.1	37.2	24.0	64.0	48.7
O	43.0	37.6	40.5	33.9	42.3	36.3	24.2	24.5
Na	0.6	0.8	0.5	0.7	0.5	0.6	0.3	0.4
Mg	0.2	0.2	0.2	0.2	0.2	0.3	0.1	0.2
P	6.8	11.5	8.2	13.3	7.4	12.3	4.4	8.6
S	0.1	0.1	0.1	0.1	0.1	0.2	0.1	0.2
Cl	0.2	0.4	0.3	0.5	0.2	0.4	0.1	0.2
Ca	11.1	24.3	13.5	28.3	12.1	25.9	6.8	17.3